Onset of convection in a finite two-dimensional container due to unipolar injection of ions

Jian Wu,[1] Philippe Traoré,[1] Pedro A. Vázquez,[2] and Alberto T. Pérez[3,*]

[1]*Institut PPRIME, Département Fluide-Thermique-Combustion, Boulevard Pierre et Marie Curie, Boîte Postale 30179,*
86962 Futuroscope-Chasseneuil, France

[2]*Departamento de Física Aplicada III, Universidad de Sevilla, ESI, Camino de los Descubrimientos s/n, 41092 Sevilla, Spain*

[3]*Departamento de Electrónica y Electromagnetismo, Universidad de Sevilla, Facultad de Física, Avenida Reina Mercedes s/n,*
41012 Sevilla, Spain

This work addresses the stability of a two-dimensional plane layer of a dielectric liquid enclosed in wall bounded cavities of different aspect ratios and subjected to unipolar injection of ions. Numerical simulations have been conducted to investigate the effect of lateral walls, especially in the development of the electroconvective instability. It is found that an unexpected change of the bifurcation nature occurs for certain cavity aspect ratios. We show that above the linear stability threshold for the rest state a supercritical bifurcation arises. This bifurcation takes place at a given value T_{c1} of the parameter T (the electric Rayleigh number). Then, a second subcritical bifurcation occurs at a second threshold T_{c2}, featuring a typical hysteresis loop with an associated nonlinear criterion T_f, which is very characteristic of the Coulomb-driven convection. This behavior has been confirmed by different numerical codes based on different numerical methods. The physical mechanism which leads to this situation is analyzed and discussed. The evolution of the bifurcation diagrams with the aspect ratio of the cavity is also provided and analyzed.

PACS number(s): 47.65.−d, 47.20.Ky, 47.11.−j

I. INTRODUCTION

The investigation of electroconvection in a dielectric liquid subjected to unipolar injection of ions has received extensive attention in the past 30 years due to its wide field of applications in major industries [1,2]. Electrohydrodynamic (EHD) ion-drag pumps [3,4], EHD turbulent mixing [5], electrostatic precipitator [6], flow control by the means of injected space charge [7,8], as well as heat transfer enhancement [9] are only a few examples of industrial applications where the Coulomb force is involved. These applications have given a new impetus to the need of deep understanding of the EHD instabilities generated by unipolar injection.

When metallic electrodes are immersed in a dielectric liquid of low enough conductivity electrochemical reactions take place at the electrode-liquid interface and injection of electric charges may occur [10]. The driving force involved in such process is the Coulomb force which acts upon the space charge injected into the bulk, the fluid being put into motion. In gases, due to the high mobility of the ions, the charges move much faster than the fluid, which means they almost follow the electric field lines. Therefore, the charge distribution is weakly coupled to the fluid flow. However, in liquids, besides the drift mechanism via the electric field, the charge is also convected by the fluid. Thus, there is a strong coupling between the hydrodynamic and the electrical effects in liquids [12]. The determination of the electric field and charge density distribution usually presents great difficulties, as the Coulomb force induced the liquid motion which, in turns, modifies the electric field and charge distributions. This nonlinear coupling as well as the complexity of the mathematical problem has prevented obtaining analytical solutions. The first authors who tackled this complex problem studied the stability of

an infinite liquid layer between two parallel electrodes and gave the foundation of the stability analysis. Several works of particular relevance for the present research, [10–13], showed the existence of a subcritical bifurcation featured by a typical hysteresis loop that occurs in such geometry.

Most of the previous studies dealt with a liquid layer that is considered infinite for the stability analysis. Only a few experimental works have been conducted and most of them are in large aspect ratio cavities [14]. The experimental studies with small aspect ratio cavities were mainly focused on the time dependent and chaotic behavior, without a detailed analysis of the instability phenomenon [15]. As a matter of fact, literature concerning wall bounded cavities in Coulomb-driven convection is relatively rare. Nevertheless, considering a fluid enclosed in a rectangular cavity of different aspect ratios is of primary importance since in most practical applications and experimental studies the liquid remains bounded by walls. There is thus a need to understand these unipolar injection-induced instabilities in this particular case.

Electrohydrodynamic (EHD) instability flows in a plane-plane configuration are analogous to the well-known Rayleigh-Bénard (RB) instability. Both of these flows are triggered by nondimensional parameters that have similar physical meaning: the Rayleigh number (Ra) in the case of RB flows and the electric Rayleigh number (T) in the case of EHD flows. In addition, both types of flows evolve in terms of similar convective patterns. However, the main difference lies on the transport mechanism of the relevant scalar magnitude: charge in the EHD case and temperature in the thermal one. While heat is mainly transported by a diffusionlike mechanism, the electric charge moves relatively to the liquid with a "drift velocity" $K\vec{E}$, where $\vec{E}$ is the electric field and K is the ionic mobility. The ion drift introduces a velocity scale in the problem that greatly influences the nature of the bifurcation, which occurs when the Rayleigh number or, respectively, the electrical Rayleigh number exceeds a critical value

*Corresponding author: alberto@us.es

(a) supercritical thermo-convective instability
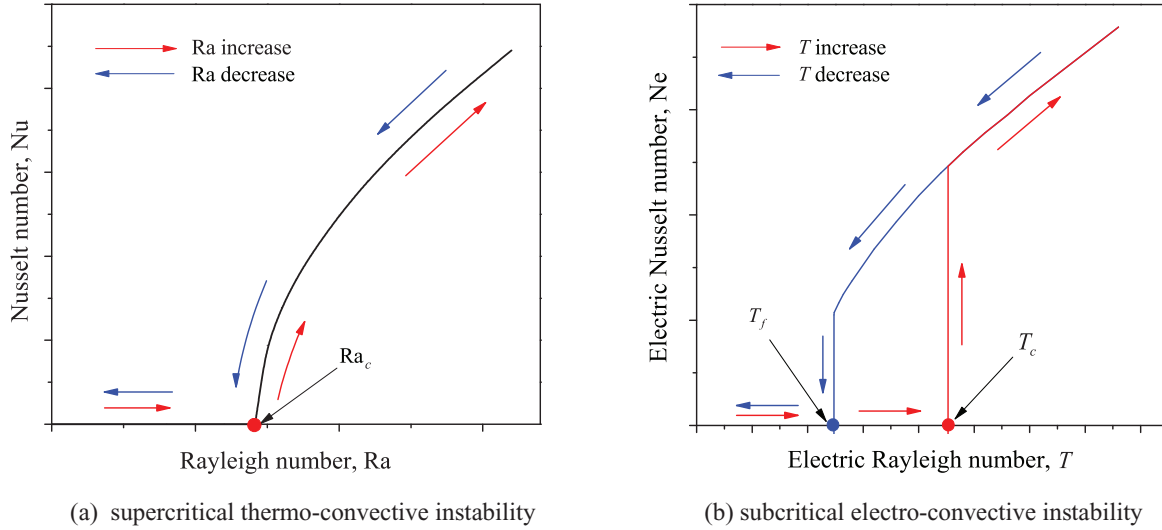

(b) subcritical electro-convective instability

FIG. 1. (Color online) Bifurcation diagrams in the Rayleigh-Bénard problem and in the electroconvective problem. Nusselt number (Nu) is defined as the ratio of the total heat flux to conductive flux, while the electric Nusselt number (Ne) is defined as the ratio of the total current to current without motion.

($\mathrm{Ra}_c = 1708.8$ in Rayleigh-Bénard flows [16] and $T_c = 164.1$, for the strong injection case [11], in electroconvective flows). The diffusion mechanism in the case of thermoconvection leads to a smooth and continuous transition between the hydrostatic state and convection [see Fig. 1(a)]. This is referred to as a supercritical bifurcation. On the other hand, the nonlinear coupling between charge, electric field, and liquid motion results first in a sudden jump between the rest state and the motion state of the liquid with a maximum velocity that exceeds the ion drift velocity [see Fig. 1(b)]. Once the motion takes place for a $T > T_c$ (the linear or small amplitude criterion), decreasing the value of T back to T_c does not result in recovering the rest state. The motion is sustaining until we reach a second criterion (nonlinear or finite amplitude criterion) T_f [see Fig. 1(b)]. A hysteresis loop links the linear and nonlinear criteria, which is a characteristic of the subcritical bifurcation.

Once the liquid is set up in motion, its maximum velocity is greater than the ionic drift velocity. As a result there appear regions where the ascending ions cannot surmount the descending liquid column, and these regions remain void of charge. The void region has been recognized to be responsible for the hysteresis loop [17]. Indeed even when T is just below T_c this region free of charges will sustain the electric torque and thus the convective motion. It is only when the electric torque becomes lower than the viscous one that the motion will stop. This nonlinear instability mechanism was derived by Felici [9] with his hydraulic model in the case of weak injection between two parallel plates. Later Atten and Lacroix [13] extended the foregoing simplified model of Felici to the case of hexagonal cells and studied the nonlinear stability problem with a Galerkin-type method. They successfully predicted the existence of a nonlinear stability criterion as well as a hysteresis loop associated with the discontinuities in current and liquid velocity. The existence of this hysteresis loop has been confirmed experimentally [13] and numerically by Castellanos and Atten [18], Chicón *et al.* [19], Vázquez *et al.* [20–22], and Traoré *et al.* [23–25].

Until now this subcritical bifurcation was known to be the main characteristic feature of electroconvective flows. However, the presence of lateral walls leads to some unique consequences. On the one hand it enhances the viscous effects, increasing the value of the instability threshold and of its associated wave number. On the other hand it promotes the appearance of secondary vortices near the cavity corners. We will show later that these secondary vortices play an important role in the overall flow structure. In this paper we shall highlight that, when the fluid is enclosed in a rectangular cavity of small aspect ratio, a supercritical branch arises before the classic subcritical bifurcation takes place. Some hints will be proposed to explain the underlying physical mechanism which leads to this unusual and unexpected behavior.

The remainder of this paper is organized as follows. In the following section the statement of the problem and the numerical methods which have been used to conduct the computations are described. Then in Sec. III we provide the different observations related to the presence of lateral walls in the domain and give a detailed analysis of the different bifurcations encountered. Finally the conclusion is given in Sec. IV.

II. STATEMENT OF THE PROBLEM AND NUMERICAL PROCEDURES

A. Basic governing equations

The system considered in this paper is a two-dimensional (2D) liquid layer of width H, assumed to be incompressible, Newtonian, and perfectly insulating, enclosed between two electrodes of length L (see Fig. 2). This layer is subjected to a potential difference $\Delta V = V_0 - V_1$. In this study, we assume that charges are injected only from the lower electrode into the bulk liquid (*unipolar* injection).

Taking as units the interelectrode spacing H for length, the applied difference voltage ($V_0 - V_1$) for electric potential, $\frac{K(V_0 - V_1)}{H}$ for velocity, $\frac{\rho K^2 (V_0 - V_1)^2}{H^2}$ for pressure, $\frac{H^2}{K(V_0 - V_1)}$ for
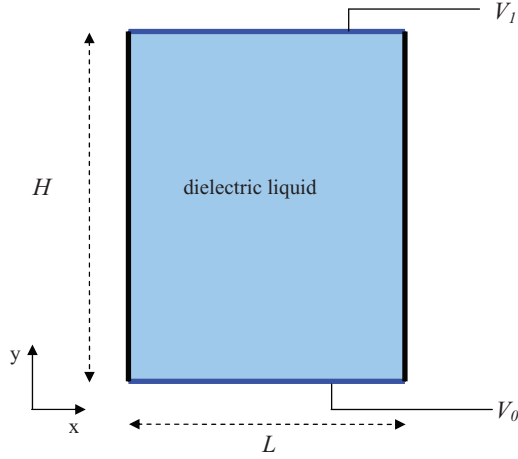
FIG. 2. (Color online) Sketch of the physical domain.

FIG. 3. Computational domain and associated numerical boundary conditions.

time, and q_0, the charge density at the injector, for charge density, the nondimensional set of classical EHD governing equations reads as [12,26]

$$\vec{\nabla} \cdot \vec{u} = 0, \tag{1}$$

$$\frac{\partial \vec{u}}{\partial t} + (\vec{u} \cdot \vec{\nabla})\vec{u} = -\vec{\nabla} p + \frac{1}{R}\Delta \vec{u} + CM^2 q\vec{E}, \tag{2}$$

$$\frac{\partial q}{\partial t} + \vec{\nabla} \cdot [q(\vec{u} + \vec{E})] = 0, \tag{3}$$

$$\Delta V = -Cq, \tag{4}$$

$$\vec{E} = -\vec{\nabla} V, \tag{5}$$

where $\vec{u} \equiv [u,v]$ is the fluid velocity and q is the charge density. p denotes the generalized pressure including the electrostriction term and the hydrostatic pressure. It should be noted that the diffusion term in Eq. (3) has been safely neglected [27]. The fluid is assumed to be homogeneous and isothermal. Under these assumptions only the Coulomb force, $q\vec{E}$, acts on the fluid. These scaling choices lead to the following set of dimensionless numbers:

$$T = \frac{\varepsilon \Delta V}{\rho_0 \nu K}, \quad C = \frac{q_0 H^2}{\varepsilon \Delta V}, \quad M = \frac{1}{K}\left(\frac{\varepsilon}{\rho_0}\right)^{1/2}, \quad R = \frac{T}{M^2}.$$

T represents the ratio of Coulomb to viscous forces, C is a dimensionless measure of the injection level, and M is the ratio between the so-called hydrodynamic mobility and the true mobility of ions [12]. To these parameters we have to add the aspect ratio $A = L/H$ of the cavity. For convenience we also define the electric Reynolds number R. In these dimensionless numbers ρ_0 is the fluid density, ν is the kinematic viscosity, and ε is the permittivity.

We further assume the injection to be *homogeneous* and *autonomous*, which means that the injected charge density at the emitter electrode is constant in time and always equal to q_0. In other words, the injector and the injection rate are neither influenced by the electric field nor by the liquid motion. It is also assumed that the ions discharge instantaneously once they reach the collector electrode.
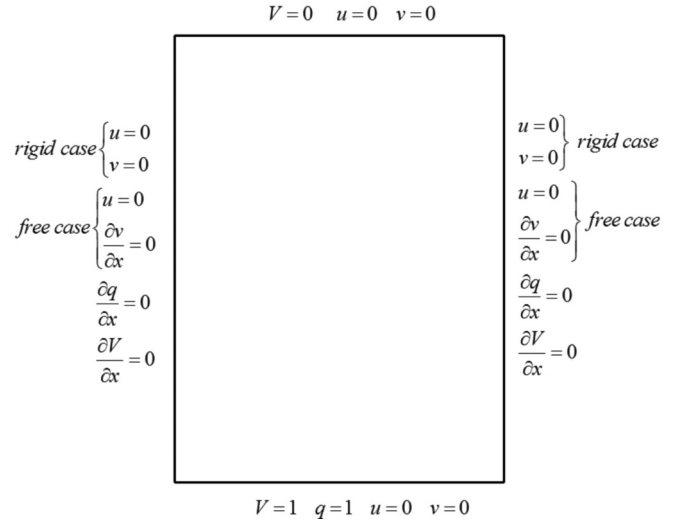
B. Numerical procedure

The numerical procedure is based on a full and direct integration of the coupled set of governing equations following a second order in time and space finite volume method [28]. The charge density transport equation, which requires a special treatment due to its hyperbolic nature, is solved using total variation diminishing (TVD) schemes [29]. The implementation of TVD schemes is to prevent spurious numerical oscillations and preserve sharp gradients and bounded solution. The interested readers may refer to [24,30] for additional details.

We have verified the main results with an alternative method based on a combined method of the discontinuous Galerkin finite element technique (DG-FE, for the charge transport equation) and continuous Galerkin finite element methods (CG-FE, for the electric and velocity fields). DG-FE has been proved to be also very efficient to deal with hyperbolic problems when sharp gradients are present. The details can be found in Ref. [22], where they have been successfully applied to EHD convection problems very recently.

The boundary conditions associated to the free and bounded electroconvection problem are depicted in Fig. 3. No-slip boundary conditions are applied on all cavity boundaries (denoted *rigid case*) except in the case of the reference solution where symmetric boundary conditions have been considered to reproduce the results of the linear stability analysis (denoted *free case*). In dimensionless form, the computational domain is defined by $0 \leqslant x \leqslant A$ and $0 \leqslant y \leqslant 1$.

III. RESULTS AND DISCUSSION

A. Free versus rigid walls: Differences in the flow structure

The most striking feature of the electroconvection in a closed box is that the loss of stability from the rest state may take place through a supercritical bifurcation, in contrast to the free walls case, where the bifurcation is always subcritical independently of the width of the container. Figure 4 illustrates this difference. It shows the bifurcation, in the strong injection case ($C = 10$), for free and rigid sidewalls and
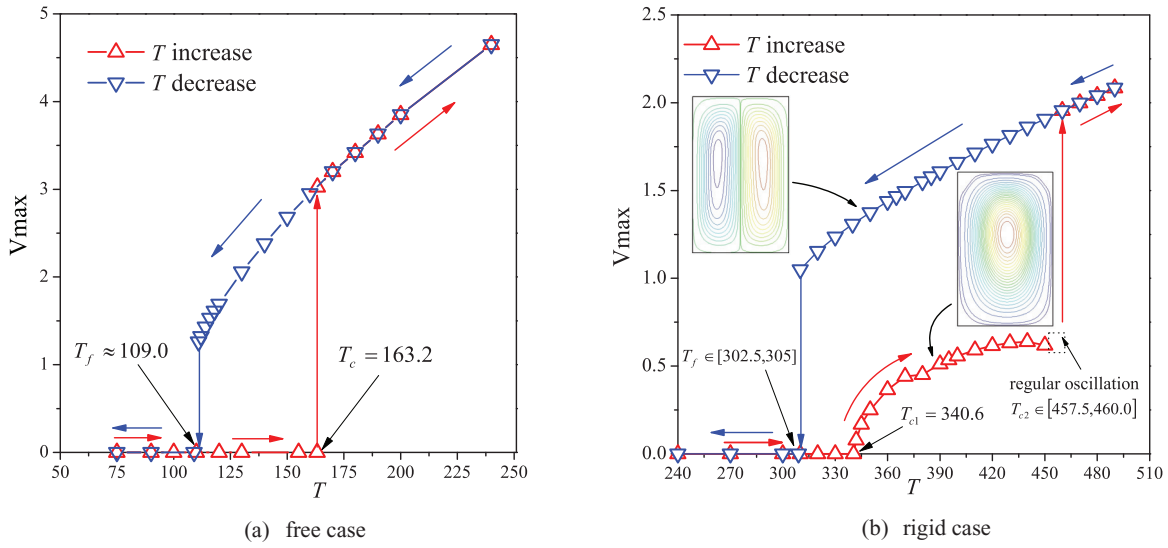
(a) free case

(b) rigid case

FIG. 4. (Color online) Bifurcation diagram for the (a) free and (b) rigid cases for $A = 0.614$.

$A = 0.614$ (the mobility parameter M is fixed as 10 in all these computations; its value does not have an important influence in the bifurcation diagrams). This particular value of A corresponds to the half wavelength of the most unstable mode in the free sidewalls case. Figure 4(a) displays the classical and expected hysteresis loop featuring a subcritical bifurcation. The computed nonlinear criterion is $T_f \approx 109$ while the linear criterion is $T_c = 163.2$. (These values are to be compared with those obtained from the nonlinear and linear stability analysis which gives, respectively, 111.7 and 164.1 [10,13]. This is so because the free sidewalls boundary conditions are the same as periodic boundary conditions, which is equivalent to the Fourier expansion made in the linear stability analysis.) In Fig. 4(b) we present the bifurcation diagram in the *rigid walls*

case. We observe two bifurcations: a supercritical bifurcation, at the point where the rest state loses its stability, with a first threshold T_{c1}, and a second bifurcation, which is subcritical, with a threshold T_{c2}. Between these two values the flow consists of one roll with secondary vortices near the corners. Since the viscous effect is enhanced by the presence of the sidewalls, the threshold $T_{c1} = 340.6$ is notably greater than the corresponding value in the *free walls case*. At the end of the supercritical branch, when the second threshold is reached (in this case we obtain $T_{c2} \in [457.5, 460.0]$) there is a sudden jump with the development of a subcritical bifurcation. For $T > T_{c2}$ the maximum velocity is always greater than the ion drift velocity, and a hysteresis loop appears: If we decrease T, the motion is sustained until we reach the nonlinear criterion

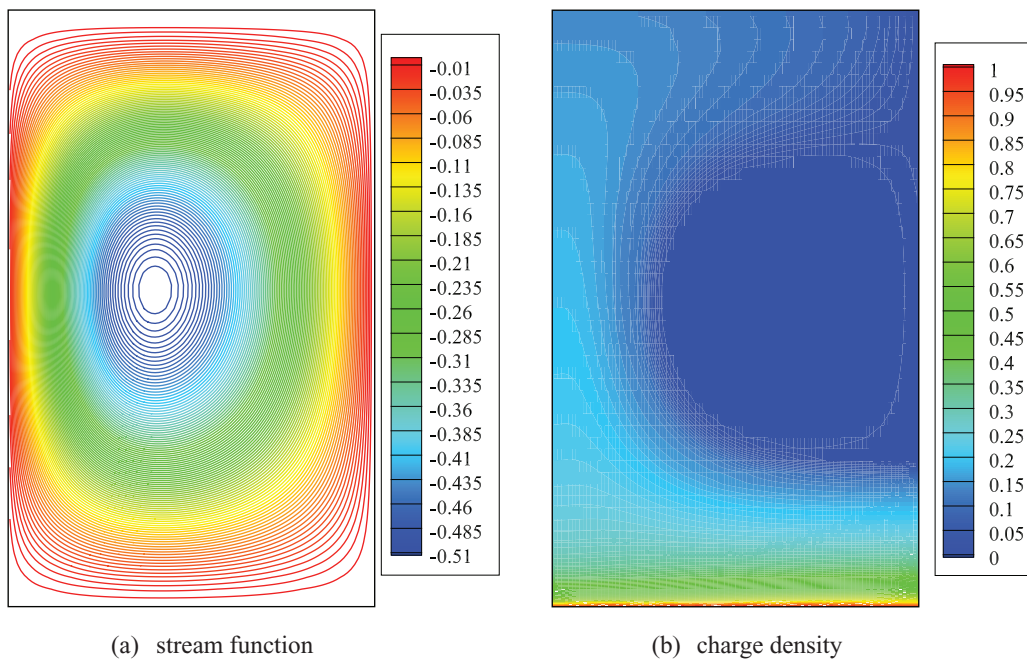(a) stream function

(b) charge density

FIG. 5. (Color online) Stream function and charge density distribution for $T = 180$ and $A = 0.614$ in the *free* case.

$T_f \in [302.5, 305.0]$. Along this upper branch the flow presents two rolls. The mechanism that leads to the existence of a hysteresis loop is similar to the one observed in the *free case* and was already described in the Introduction.

Let us examine the flow structure to understand what could lead to this unexpected behavior. Figure 5 shows the stream function distribution and isocontour lines of the charge density for the free walls case. When T is slightly above the critical value T_c the motion starts in the form of one convective roll as it is seen on the stream function distribution [Fig. 5(a)]. The charge density is greater in the regions where the liquid is ascending and smaller in the regions where the liquid is descending. This is a consequence of the fact that the charge density evolves following the law [27]

$$q(x,y) = \frac{1}{1 + Ct},$$

where t is the time needed for a charge carrier to reach the point (x, y). Wherever the velocity goes from the injector to the collector, the value of t is smaller than the one in the motionless state, and the charge density is greater than the motionless value. Conversely, at the points where the liquid goes from the collector to the injector, the charge density increases. At the points where the liquid velocity is equal to the ion drift velocity the charge carrier takes an infinitely long time to get there, the charge density becomes zero, and there appears a region void of charge. This is always the situation for the free sidewalls case, and a region void of charge is clearly observable in Fig. 5(b). Taking a line of $y =$ constant, i.e., a horizontal line in the figure, the charge gradient always takes the same sign, and goes from the region where the liquid moves towards the injector to the region where it moves towards the collector. This gradient produces an electrical torque that promotes the motion in the same sense of the velocity roll that has produced it. The balance between the electrical torque and the viscous one determines the amplitude of the velocity roll.

For rigid walls, it turns out that the flow pattern is more complex than a single-roll structure. First of all, due to the presence of walls, we notice some secondary vortices near the four corners. As is visible on Fig. 6, these vortices increase their angular velocities as well as their sizes when T increases. These vortices are more pronounced in the left side of the cavity since the primary vortex is clockwise rotating. The charge density distribution shown in Fig. 6 is also quite different from the free wall case. Since the liquid velocity is zero at the walls, the time of flight of ions on the lateral walls is weakly perturbed by the flow. Close to the left wall in Fig. 6 ($T \leqslant 430$) the liquid goes towards the injector, and the charge density decreases in this region. On the right side the liquid moves towards the collector and the charge density increases, but again, at the right wall it is smaller. Contrary to the free wall case, the charge density gradient along a horizontal line
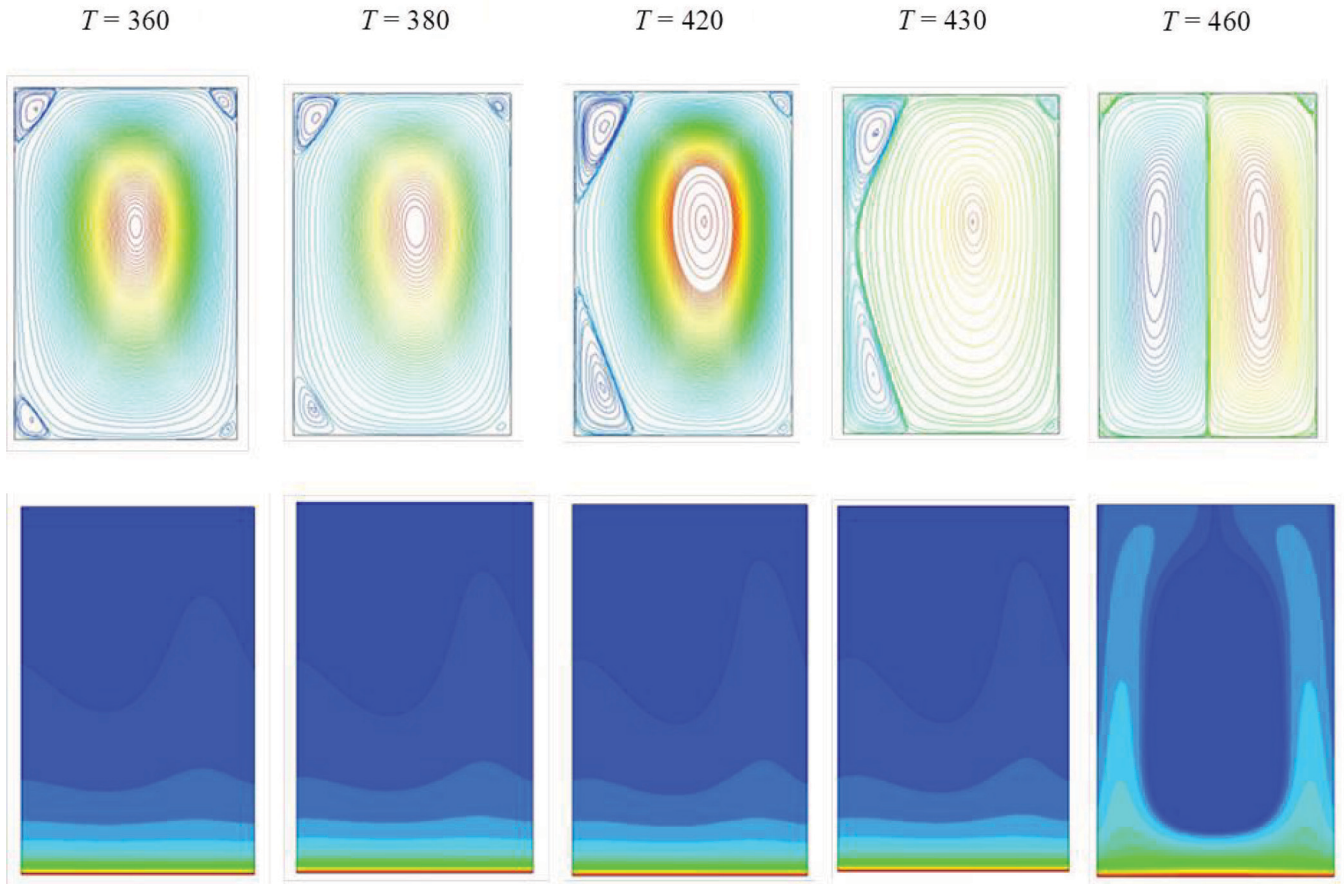
| $T = 360$ | $T = 380$ | $T = 420$ | $T = 430$ | $T = 460$ |

FIG. 6. (Color online) Stream function and isocontours of the charge density distribution for different T values in the *rigid* walls case ($A = 0.614$, $C = 10$).

changes sign. Although the overall electric torque promotes the motion of the principal roll, the gradient on the left boundary tends to induce a counter-rotating roll, and decelerates the principal one. Therefore, the presence of the walls changes the charge density distribution in a way that weakens the initial roll and enhances the secondary vortices.

As long as we stay on the supercritical branch, i.e., for $T \in [340.6, 460.0]$, only one primary vortex is observed. When the secondary vortices seem to join, the flow becomes very unstable and the two secondary vortices on the left side (see Fig. 6) merge together to form a primary vortex. At this stage we observe two primary vortices and four secondary ones. This bifurcation is subcritical and occurs for a T in the range of $[457.5, 460]$. It is worth noting that for $T < 457.5$ no region free of charge is observed, which explains why the first bifurcation at $T = 340.6$ is supercritical. When T exceeds 460 a region free of charge is formed and the bifurcation turns out to be a subcritical type.

The bifurcation diagram for rigid walls, as compared to the free walls case, may be ascribed to the growth of the secondary vortices near the corners and the presence of the walls, which originates additional gradients of charge in the volume.

B. Small amplitude behavior

In order to better understand the behavior of the electroconvection due to unipolar injection in a closed 2D box when varying the aspect ratio, it is worthwhile to have a look at the small velocity amplitude behavior that corresponds to the linear stability analysis. Figure 7 shows the linear stability threshold as a function of A for the free walls case as obtained from a linear stability analysis similar to the one used by Atten and Moreau [11].

The number on every branch corresponds to the number of rolls that appear at the instability threshold. For $n = 2$ the minimum value of T_c is found at $A = 1.228$, exactly twice the value for $n = 1$, and the value of T_c is the same. For $n = 3$, the same minimum value of T_c is found at A equal to 3 times the value of A for the minimum for $n = 1$, and so on. This is due to the fact that the structure for n rolls consists in n copies of the structure for one roll. The same plot was obtained numerically in Ref. [24].

Things are different for the rigid walls case. Figure 8 shows the linear stability criterion for rigid walls and the same
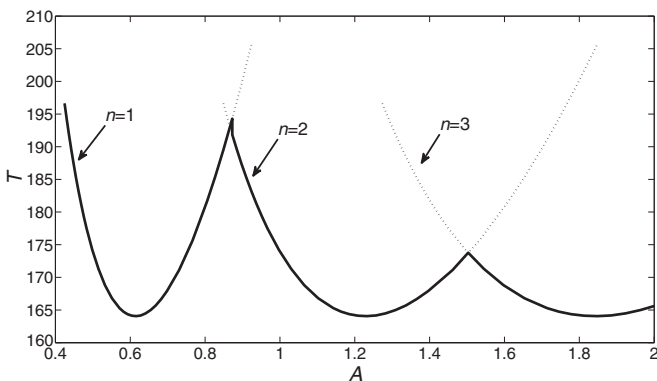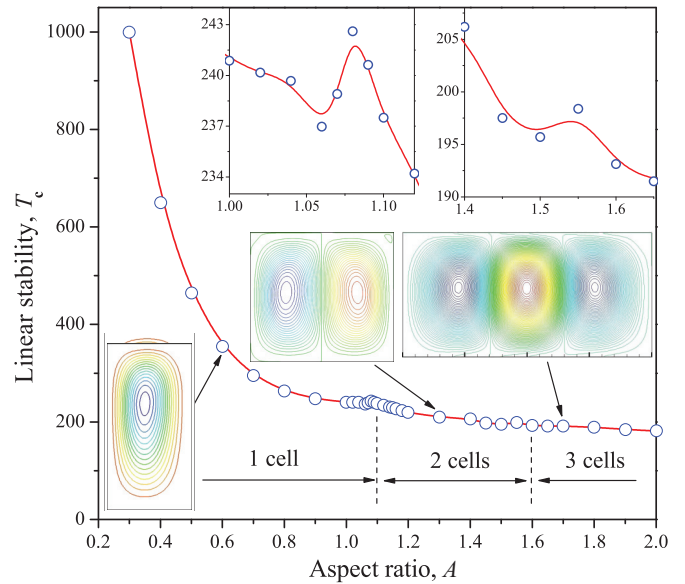

FIG. 8. (Color online) Linear stability criteria T_c versus the aspect ratio A for $C = 10$ in the *rigid* walls case.

nondimensional parameters as Fig. 7. A nonsmooth curve with humps is obtained. The labels indicate the number of rolls in every section of the curve. First of all, we observe that the first minimum corresponds to a higher value of T than for the free wall case, something we have already noted in the previous section and it is related to the stabilizing effect of the walls. Also the value of A for the minimum is greater than in the free wall case. Another difference is that the minimum of the curve for $n = 2$ does not correspond to the same value of T than for $n = 1$, neither to a double value of A. This is due to the fact that the structure of two rolls in this case is not the duplicate of a single-roll structure. For two rolls, the y component of the velocity is different from zero at the center, whereas it would be zero if we duplicate the one-roll structure for rigid walls.

In the same figure, the flow structure is displayed in the early stage of the growing instability process, i.e., when the dimensionless velocity is very small, for example, of the order of 0.01. As is expected from the discussion in the previous section, the rolls are not simple structures, but they have small vortices near the corners. Near the cusps in the curve T versus A, where modes of different number of rolls may coexist, competition between two modes is expected.

All these characteristics of the linear or small amplitude behavior are very similar to the ones found in Rayleigh-Bénard and Marangoni problems for the stability analysis in finite wall bounded containers [31–36].

C. Detailed bifurcation analysis

Depending on the value of the aspect ratio supercritical or subcritical bifurcations may appear. Figure 9 shows the values of the three stability thresholds for T as a function of A. For $A < 1.05$, there is a first supercritical bifurcation followed by a subcritical one. The evolution of the flow structure is depicted in Fig. 6: First there is a main roll with small asymmetric vortices in the corner, the vortices on the left side grow, and,
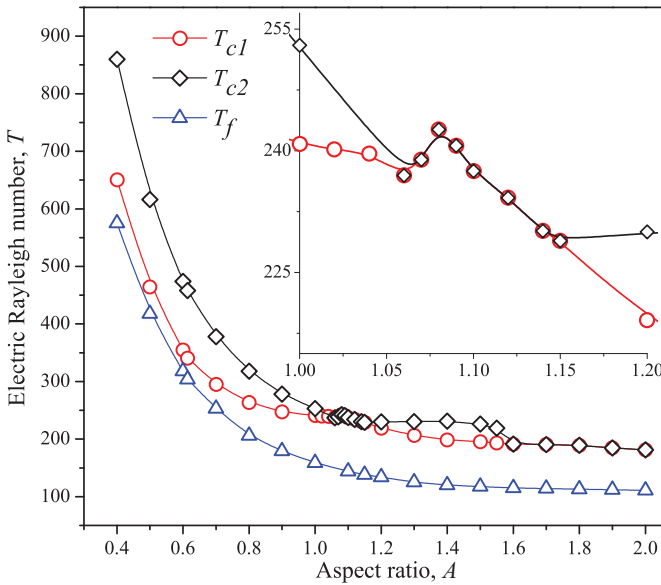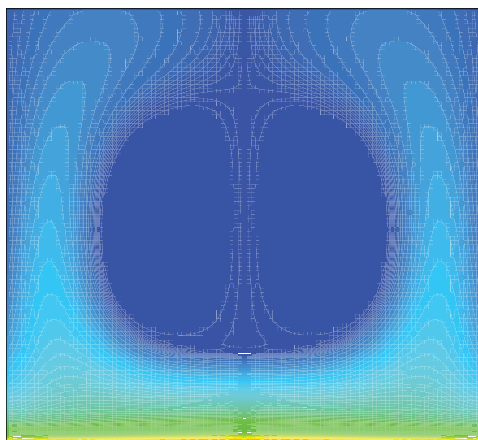

FIG. 7. Linear stability criterion T_c versus A for $C = 10$ in the *free* case.

FIG. 9. (Color online) Linear and nonlinear stability thresholds versus the aspect ratio for the *rigid* walls case.

FIG. 11. (Color online) Bifurcation diagram in the *rigid* walls case with $A = 1.4$.

finally, two rolls develop when the second instability threshold T_{c2} is overcome.

For $A \in [1.05, 1.15]$, the supercritical behavior disappears and T_{c1} and T_{c2} merge. It is reasonable to think that this point corresponds to the merging of the first and second unstable modes in the linear stability analysis. In this range, the charge void region is formed with T slightly higher than the linear stability threshold. An example with $A = 1.1$ and $T = 245.0$ (for this aspect ratio, $T_{c1} = T_{c2} = 237.5$) is provided in Fig. 10.

For $A > 1.15$, the supercritical behavior is reencountered, but the flow structure is different: It starts with two rolls that persist after the second instability threshold T_{c2}. Figure 11 shows the complete bifurcation diagram with $A = 1.4$ for this case. It should be noted that the supercritical bifurcation is not symmetrical with respect to the sense of rotation of the rolls. This is in contrast with the findings for $A < 1.05$. For a single-roll structure the flow and the charge distribution are symmetrical along a vertical axis. The structure is the
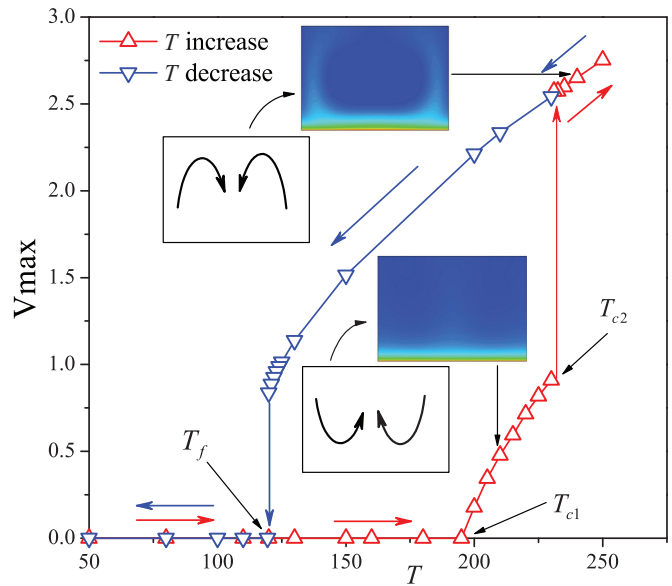
same if the flow is clockwise rather than counterclockwise. For two rolls and rigid walls, this symmetry is broken and the charge distribution is not the same when the liquid goes from the injector to the collector at the center as when it goes in the opposite direction. One consequence of this symmetry breaking is that the slope of V_{max} versus T is not infinity at the bifurcation point. There are two rolls in the supercritical branch as well as in the upper branch. However, the sense of rotation of the rolls is the opposite. In the supercritical branch, where the maximum velocity is always smaller than the ion drift velocity, the liquid goes towards the collector at the center of the cell. In the upper branch, where the maximum velocity is greater than 1, the liquid at the center goes towards the injector. In this case there is a region void of charge at the center of the cell (see Fig. 11).

If we start a simulation for a value of $T > T_{c2}$ taking as initial condition a solution with a value of $T < T_{c2}$, the transition between both structures takes place on the

(a) charge density
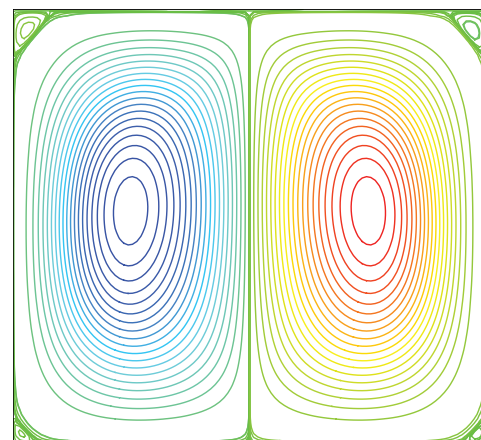
(b) stream function

FIG. 10. (Color online) Isocontour lines for charge distribution and stream function with $A = 1.1$ and $T = 245.0$ in the *rigid* walls case.

(a) charge density

(b) stream function

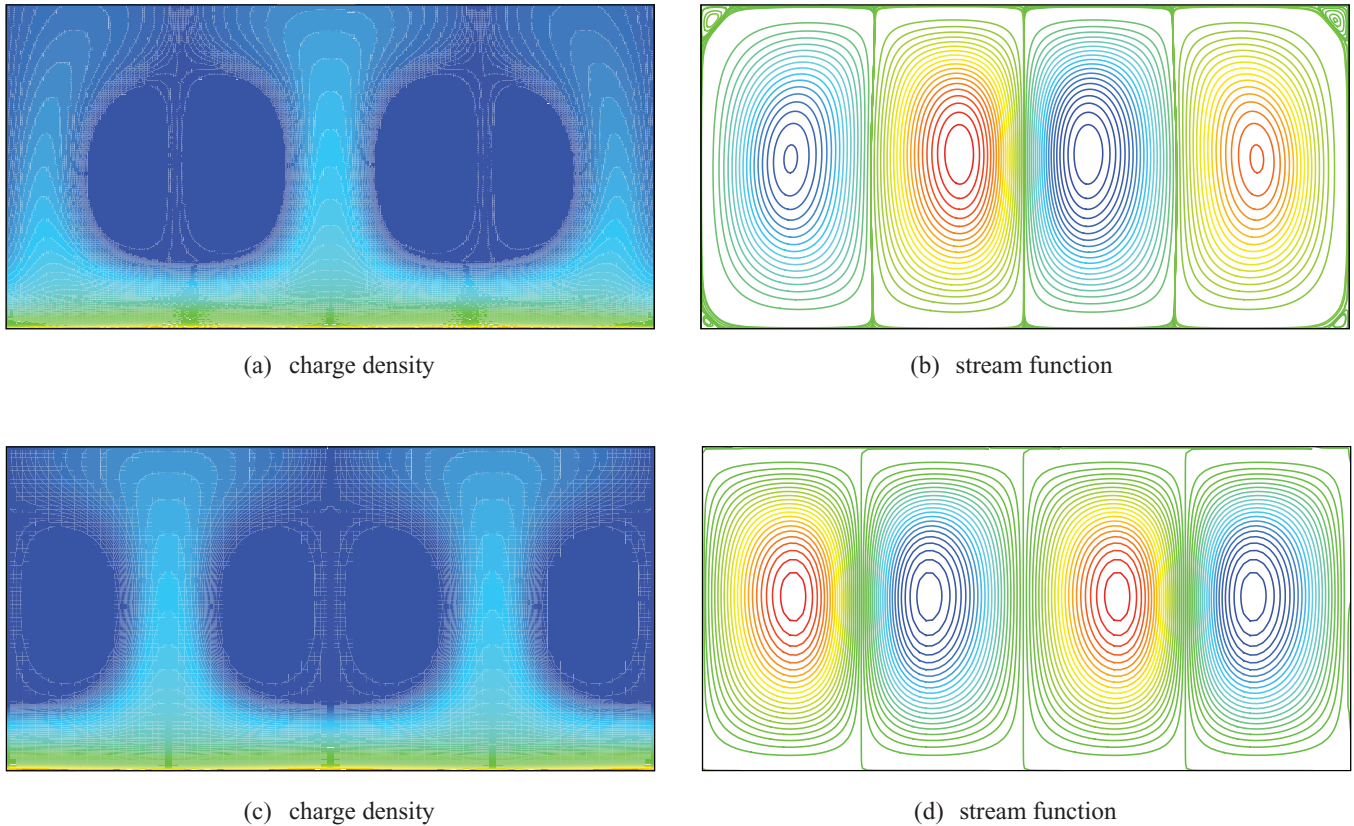(c) charge density

(d) stream function

FIG. 12. (Color online) Isocontour lines of charge distribution and stream function with $A = 2.0$ and $T = 200$: (a) and (b) with *rigid* walls; (c) and (d) with *free* walls.

supercritical branch. During this transition the vortices on the left corners of the domain grow in time, then merge into one roll; at a certain time there are three rolls. However, these three rolls are not stable. The rolls move towards the right and the one on the right disappears, leaving a two-roll structure, but with the sense of rotation inverted. It is worth pointing out that when the liquid velocity is greater than 1 we always observe an even number of rolls, with a region void of charge between two rolls.

For $A \geqslant 1.6$, the bifurcation is always subcritical. The flow structure corresponds to an even number of rolls. The influence of the vertical walls starts to weaken and the situation is more and more like the expected for free walls or an infinite container. For $A \gg 1.0$, the linear and nonlinear criteria tend to the free wall values. Figure 12 shows a comparison of the results for rigid and free walls for $A = 2.0$ and $T = 200.0$. Apart from a half-wavelength translation, both structures are very similar. Some computations have been conducted for a large domain with $A = 10.0$. In this case $T_{c1} = T_{c2} = 164.3$ and $T_f \approx 110.0$, which are very close to the values obtained by the stability analysis with free walls. This clearly shows that the wall effect vanishes for such aspect ratio.

IV. CONCLUSION

In this article numerical simulations have been undertaken to highlight the existence of a supercritical bifurcation which arises in Coulomb-driven convection in wall bounded cavities.

It has been shown that in a small cavity, the electroconvective instability develops first in a supercritical bifurcation when the control parameter T, the electrical Rayleigh number, is above a first critical value T_{c1}. When a second critical value $T_{c2} > T_{c1}$ is reached, the well-known and expected subcritical bifurcation develops. For large aspect ratios the difference $(T_{c2} - T_{c1})$ vanishes and a more classical routine is recovered. These two small amplitude criteria as well as the finite amplitude criterion T_f are dependent on the aspect ratio of the cavity, A. The bifurcation structure also depends on A. For $A < 1.05$, there is only one roll in the supercritical branch, that gives place to a two-roll structure after the second bifurcation. For $1.15 < A < 1.6$, the supercritical branch presents a two-roll structure that is replaced, after the second bifurcation point, by another two-roll structure, but with an inversion in the sense of rotation. For $1.6 \leqslant A$ the supercritical bifurcation disappears, recovering the behavior of the free wall case.

[1] J. M. Crowley, *Fundamentals of Applied Electrostatics* (Wiley, New York, 1986).

[2] J. R. Melcher, *Continuum Electromechanics* (The MIT Press, Cambridge, MA, 1981).

[3] J. Seyed-Yagoobi, J. E. Bryan, and J. A. Castaneda, IEEE Trans. Ind. Appl. **31**, 469 (1995).

[4] J. Seyed-Yagoobi, J. Electrost. **63**, 861 (2005).

[5] M. Jalaal, B. Khorshidi, and E. Esmaeilzadeh, Chem. Eng. J. **219**, 118 (2013).

[6] K. Adamiak and P. Atten, in *6ème Conférence de la Société Française d'Electrostatique, Paris & Gif-sur-Yvette* (Société Française d'Electrostatique, Paris, 2008), pp. 188–193.

[7] P. Traoré, M. Daaboul, and C. Louste, J. Phys. D: Appl. Phys. **43**, 225502 (2010).

[8] C. Louste, Z. Yan, P. Traoré, and R. Sosa, J. Electrost. **71**, 504 (2013).

[9] F. M. J. McCluskey, P. Atten, and A. T. Pérez, Int. J. Heat Mass Transfer **34**, 2237 (1991).

[10] N. Félici, Revue Géneral d'Electricité **78**, 717 (1969).

[11] P. Atten and R. Moreau, J. Mec. **11**, 471 (1972).

[12] P. Atten, IEEE Trans. Dielectr. Electr. Insul. **3**, 1 (1996).

[13] P. Atten and J. C. Lacroix, J. Mec. **18**, 469 (1979).

[14] P. Atten, J. C. Lacroix, and B. Malraison, Phys. Lett. A **79**, 255 (1980).

[15] B. Malraison and P. Atten, Phys. Rev. Lett. **49**, 723 (1982).

[16] S. Chandrasekhar, *Hydrodynamic and Hydromagnetic Stability* (Oxford University Press, Oxford, UK, 1961).

[17] A. Castellanos, P. Atten, and A. T. Pérez, PhysicoChem. Hydrodyn. **9**, 443 (1987).

[18] A. Castellanos and P. Atten, IEEE Trans. Ind. Appl. **IA-23**, 825 (1987).

[19] R. Chicón, A. Castellanos, and E. Martín, J. Fluid Mech. **344**, 43 (1997).

[20] P. A. Vázquez, G. E. Georghiou, and A. Castellanos, J. Phys. D: Appl. Phys. **39**, 2754 (2006).

[21] P. A. Vázquez, G. E. Georghiou, and A. Castellanos, J. Phys. D: Appl. Phys. **41**, 175303 (2008).

[22] P. A. Vázquez and A. Castellanos, Comput. Fluids **84**, 270 (2013).

[23] P. Traoré, A. T. Pérez, D. Koulova-Nenova, and H. Romat, J. Fluid Mech. **658**, 279 (2010).

[24] P. Traoré and A. T. Pérez, Phys. Fluids **24**, 037102 (2012).

[25] P. Traoré and J. Wu, J. Fluid Mech. **727**, R3 (2013).

[26] A. Castellanos, IEEE Trans. Dielectr. Electr. Insul. **26**, 1201 (1991).

[27] A. T. Pérez and A. Castellanos, Phys. Rev. A **40**, 5844 (1989).

[28] S. V. Patankar, *Numerical Heat Transfer and Fluid Flow* (Hemisphere, Washington, DC, 1980).

[29] P. K. Sweby, SIAM J. Numer. Anal. **21**, 995 (1984).

[30] J. Wu, P. Traoré, and C. Louste, J. Electrost. **71**, 319 (2013).

[31] A. I. Van de Vooren and H. A. Dijkstra, Comput. Fluids **17**, 467 (1989).

[32] K. H. Winters, Th. Plesser, and K. A. Cliffe, Physica D **29**, 387 (1988).

[33] I. Canton, Int. J. Heat Mass Transfer **15**, 665 (1972).

[34] A. Yu. Gelfgat, J. Comput. Phys. **156**, 300 (1999).

[35] H. A. Dijkstra, J. Fluid Mech. **243**, 73 (1992).

[36] J. Mizushima, J. Phys. Soc. Jpn. **64**, 2420 (1995).